ELSEVIER

Contents lists available at ScienceDirect

# Estuarine, Coastal and Shelf Science

journal homepage: www.elsevier.com/locate/ecss





# Comparison of structure and turbulent mixing between lateral and leading-edge river plume fronts: Microstructure observations from a T-REMUS AUV

Nikiforos Delatolas <sup>a, 1</sup>, Daniel G. MacDonald <sup>a, \*</sup>, Louis Goodman <sup>a</sup>, Michael Whitney <sup>b</sup>, Kimberly Huguenard <sup>c</sup>, Kelly Cole <sup>c</sup>

- <sup>a</sup> University of Massachusetts Dartmouth, United States
- <sup>b</sup> University of Connecticut, United States
- c University of Maine, United States

#### ARTICLE INFO

Keywords:
River plume
Turbulence
Autonomous underwater vehicle

#### ABSTRACT

The energetic frontal region of the tidally pulsed Connecticut River plume was sampled with the T-REMUS Autonomous Underwater Vehicle (AUV) which navigated ten cross-front transects at various depths. Synchronous and high resolution hydrographic, microstructure, velocity and backscatter observations allowed the creation of detailed views of frontal structure and turbulent mixing in the reference frame of the propagating front. The front was defined by a sharp horizontal density gradient of  $\sim$ 18.5 kg m $^{-4}$  across only 0.7 m in the horizontal, and strong downwelling velocities of 0.17 m/s. Three successive zones were consistently identified. The first O (10 m) wide downwelling zone in which buoyant plume water was forced downward, thereby forming a highly energetic frontal head that extended down to 6 m depth and had TKE dissipation rates ( $\epsilon$ ) of order  $10^{-3}$  m<sup>2</sup>/s<sup>3</sup>. Beyond the downwelling zone to O (100 m), a transition zone was observed, characterized by substantial entrainment of ambient water. This zone had high amplitude and high frequency density anomaly ( $\sigma_0$ ) variability consistent with elevated but decreasing turbulent kinetic energy dissipation rates (ε) which ranged between 10<sup>-1</sup> and  $10^{-5}~\text{m}^2/\text{s}^3$ . Beyond O (100 m) from the front, stable stratification, high Ri values, and low Re<sub>b</sub> values, suppressed the growth of instabilities and diminished turbulent mixing. In this stable interior region the plume base shoaled to 2 m depth and  $\varepsilon$  decreased further, from  $10^{-5}$  to  $10^{-7}$  m<sup>2</sup>/s<sup>3</sup>. In ambient Long Island Sound waters,  $\epsilon$  ranged between  $10^{-6}$  and  $10^{-7}$  m<sup>2</sup>/s<sup>3</sup>. The cross-front distributions of  $\sigma_{\theta}$  and  $\epsilon$  did not change substantially as the front transformed from a lateral boundary, where plume flow was primarily in the along-front direction, to one that was at the leading edge of the plume, where plume flow was mostly in the cross-front direction. In both cases, a significant convergence was present at the front due to strong ambient tidal velocities. The observed  $\epsilon$  values and those from four previous studies of large and mid-sized plumes were nondimensionalized using the velocity and length scales associated with the downwelling region at the front. The effective normalization suggests that local dynamics primarily control  $\varepsilon$  in the near-frontal region.

# 1. Introduction

River plume fronts are features created around the perimeter of river plumes and delineate the buoyant river discharge from the coastal ocean [Horner-Devine et al., 2015]. Processes that occur at fronts are critical for understanding the overall dilution and transport of plumes. Direct observations of plumes have been conducted only at sparse temporal and/or spatial scales. Thus, a detailed description of the transport and

mixing of plume water through the frontal region is still needed [Cole et al. 2020]. Previous laboratory experiments on the dynamics and circulation of buoyant gravity currents [i.e., Britter and Simpson, 1978; Simpson and Britter, 1979; Jirka and Arita 1987], which have served as models for geophysical scale plumes, have uncovered empirical relationships between non-dimensional variables that control the behavior of the advancing current and have yielded equations for the entrainment of ambient fluid, an important product of frontal mixing. Numerous field

 $<sup>^{\</sup>star}$  Corresponding author.

E-mail address: dmacdonald@umassd.edu (D.G. MacDonald).

<sup>&</sup>lt;sup>1</sup> currently at Woods Hole Oceanographic Institution.

studies have applied results from these laboratory experiments to explain the structure and mixing at river plume fronts. However, these laboratory-generated gravity currents merely serve as models and thus provide an inherently simplistic view of the geophysical reality. In this study, we seek to address these gaps using synchronous multiscale observations from an Autonomous Underwater Vehicle (AUV) that can provide repeated high-resolution views of frontal structure and turbulent mixing.

#### 1.1. Laboratory and field observations

Simpson, 1982 conducted pioneering laboratory work studying the structure and behavior of near-steady state negatively buoyant gravity currents that were opposed by a positively buoyant uniform flow. They expanded on the flow-force theory of *Benjamin* [1968] to include mixing at the current head, and quantified non-dimensional entrainment of ambient water into the advancing current as  $= Qg'/U_1^3$ , where  $U_1$  is the relative speed between ambient flow and gravity current and Q the discharge flow rate per unit width. The reduced gravity was given by  $g' = g(\rho_2 - \rho_1)/\rho_2$  where g is the gravitational acceleration,  $\rho_1$  the density of buoyant flow, and  $\rho_2$  the density of the gravity current. The physical model on which their theory was based is shown in Fig. 1a, which assumed inviscid, incompressible, and steady flow. A mixed

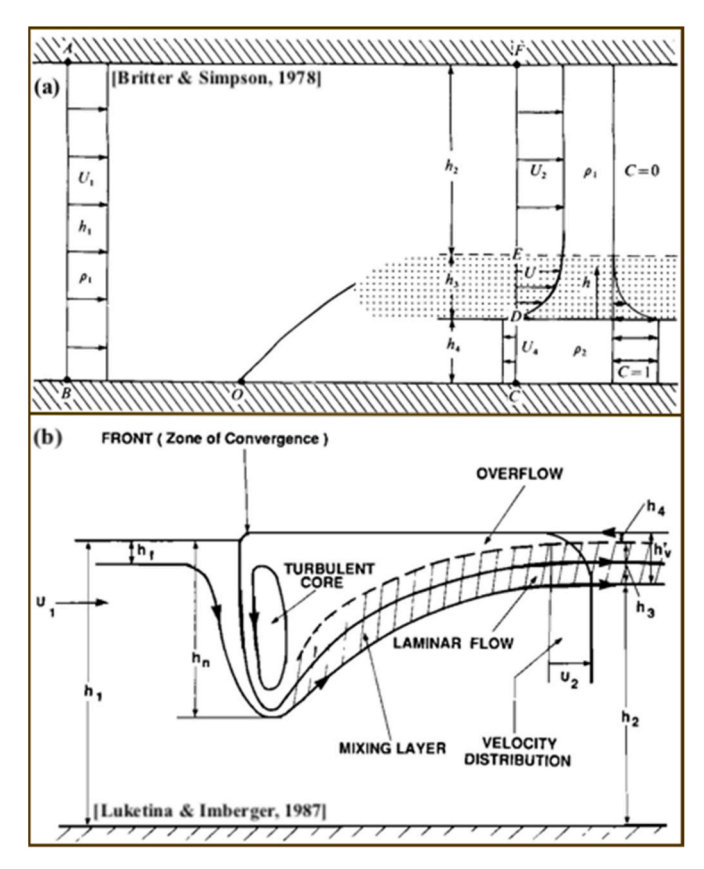


**Fig. 1.** (a) Physical model of gravity current head developed from laboratory experiments as seen in Britter & Simpson [1978]. (b) Schematic of streamline pattern in a plume front as seen in Luketina and Imberger [1987]. In both schematics, the entire water depth is denoted by  $h_1$ , the height of ambient water underneath the plume by  $h_2$ , the height of the mixing layer by  $h_3$ , and the height of flow into the gravity current head by  $h_4$ . In (b),  $h_n$  is the current head height;  $h_v$ , the current depth far away from the front; and  $h_f$ , the height of entrained fluid. In both schematics the mixed layer experiences the strongest velocity and density gradients. The two schematics are conceptually the same with velocities in both being in the reference frame of the gravity current. However, in (a) the gravity current is negatively buoyant while in (b) it is positive.

region of height  $h_3$  was defined between the gravity current and ambient fluid and enveloped the density and velocity gradients necessary to bridge the other two regions. Shadowgraphs brilliantly captured the gravity current's relatively thin laminar layer of overtaking flow and height  $h_4$  that fed into a blunt body leading head.

In a series of field studies of the Leschenault estuary buoyant outflow, Imberger, [1983], Imberger & Luketina [1987], and Luketina and Imberger [1987, 1989] compiled some of the most detailed observations of geophysical scale gravity currents and were the first to draw comparisons with the lab experiments of Britter & Simpson [1978]. Their physical model was basically a positively buoyant version of Britter & Simpson's model with additional detail on the shape and flow patterns near the frontal head (Fig. 1b). They observed a convergence and associated downwelling region with vertical velocities approximately 0.10 m/s at the plume front, below which a clearly defined head penetrated to 3 m depth. The head was found to have uniform Turbulent Kinetic Energy (TKE) dissipation rates ( $\epsilon$ ) of order  $10^{-6}$  m<sup>2</sup>/s<sup>3</sup>. Beyond 200 m behind the front, the plume gradually shallowed to a depth of about 2 m and became strongly stratified similarly to the shear-stratified region of thickness  $h_3$  seen in Fig. 1a. With increasing distance away from the front, TKE dissipation decreased to  $10^{-8}~\text{m}^2/\text{s}^3$  as stratification suppressed mixing.

The gradient Richardson number, as formulated by Ellison and Turner, 1959, is given by  $Ri_g=N^2/S^2$ , where  $N^2=g\rho_o^{-1}\partial\rho/\partial z~S^2=(\partial u/\partial z)^2+(\partial v/\partial z)^2$  squared and the horizontal velocity shear squared. Density is represented by  $\rho$ , the horizontal components of velocity by u and v, and vertical length by  $z~Ri_g~Ri_g$  signifies the competition between shear and stratification with increasing values indicating the prevalence of stabilizing buoyancy forces over destabilizing shear induced turbulence and mixing. A less than the critical value of 0.25 provides a necessary but not sufficient condition for the occurrence of Kelvin-Helmholtz instabilities [*Miles*, 1961].

Imberger & Luketina [1987] showed that the rotary-like head region of the plume had low  $Ri_g$  values around 0.1 whereas the wake region behind the head was found to have supercritical values for which the formation of instabilities may be suppressed. Thus, they suggested that turbulence generated in the head was advected into the wake, moving from a region of subcritical  $Ri_g$  to one that was supercritical. This conclusion may not be entirely true because the sparse sampling employed would not have resolved the inhomogeneity of turbulence where pockets of subcritical  $Ri_g$  might exist in a region with higher mean  $Ri_g$ .

*O'Donnell* et al. [2008] sampled the Connecticut River plume front with six cross-front transects over a 30-min period. Data showed weakening of frontal mixing and shallowing of the frontal head with increasing distance away from the river jetties. Using the Ellison overturning scale [Ellison, 1957]  $L_E$ , a representative turbulent length scale based on observed high frequency salinity variability and the local salinity gradient, they estimated  $\varepsilon$  using the formulation:

$$\varepsilon = N^3 L_E^2 / \alpha^2 \tag{1}$$

where  $\alpha$  was assumed constant at 1.5. The cross-front distribution of  $\varepsilon$  showed the highest values at the front of order  $10^{-3}~\text{m}^2/\text{s}^3$  decreasing to  $10^{-6}~\text{m}^2/\text{s}^3$  within 100 m behind the front. These data were fitted with a curve of the form  $\varepsilon(x)=\varepsilon_o\exp(-x/L_G)$  with  $L_G$  representing a decay length scale, which was found to equal approximately 15 m.

The buoyancy Reynolds number  $Re_b$  is defined as the ratio of the Ozmidov length scale,  $L_O = (\varepsilon/N^3)^{\frac{1}{2}}$ , to the Kolmogorov length scale [Kolmogorov, 1941]  $L_K = (\nu^3/\varepsilon)^{\frac{1}{4}}$ , raised to the 4/3 power:  $Re_b = (L_O/L_K)^{\frac{4}{3}} = \varepsilon/\nu N^2$ , where  $\nu$  is the kinematic viscosity. Turbulence can be considered fully developed when there are two orders of magnitude between the smallest ( $L_K$ ) and largest ( $L_O$ ) scales. This means that for  $10 < (L_O/L_K) < 100 \Rightarrow 21 < Re_b < 464$ , turbulence is transitioning to isotropy, for  $Re_b < 21$  turbulence is suppressed by strong density

gradients, and for  $Re_b > 464$  turbulence is strong and fully isotropic [*Itsweire* et al. 1986; *Iven and* Imberger, 1983].

*O'Donnell* et al. [2008] found  $Re_b$  to be at or below 16 for the entire length of the transect farthest away from the river jetties (about 1500 m). In all other transects and for a cross-front distance greater than 85 m behind the front, they also found  $Re_b \leq 16$ . This signifies that overturning turbulence, vertical mixing, and entrainment were substantially suppressed [*Itsweire* et al., 1993] behind the frontal head region and away from the river jetties. In a similar trend, Imberger & Luketina [1987], reported decreasing  $Re_b$  values with distance away from the front that became subcritical ( $Re_b < 21$ ) beyond 400 m distance, possibly implying that observed turbulent motions might become increasingly anisotropic with distance away from the front.

Orton & Jay, [2005] collected numerous CTD profiles from the Columbia River plume to measure overturn scales and estimated  $\epsilon$  as a function of distance behind the front. The estimates of TKE dissipation were given by

$$\varepsilon = N^3 L_T^2 / \alpha^2 \tag{2}$$

where  $L_T$  is the rms vertical displacement of water parcels [*Thorpe*, 1977] in each overturn patch, and  $\alpha$  approximately 1. Their measurements ranged between 50 m and 2000 m behind the front and were averaged vertically throughout the plume layer. Vertically averaged  $\varepsilon$  values ranged from  $10^{-3}$  m $^2/\text{s}^3$  at 50 m behind the front to  $10^{-6}$  m $^2/\text{s}^3$  at 1000 m behind the front. However, it does not appear that these data were adjusted for the stable portions of the water column, i.e., the volume fraction of water sampled in each profile for which overturns were not observed, which would bias dissipation estimates high. Additionally, TKE dissipation rate equations (1) and (2) describe turbulence arising from the collapse of Kelvin-Helmholtz instabilities and thus, they may not be valid in cases where turbulence is generated from convective processes, or they may be insufficient when turbulence is advected from other regions.

#### 1.2. Current limitations in understanding

As summarized above, extensive efforts have been dedicated to better understanding the dynamics and structure of buoyant plume fronts, as well as the temporal and spatial evolution of frontal structure and hydrography [i.e., Garvine and Monk, 1974; Luketina and Imberger, 1987; O'Donnell et al., 2008; Jirka and Arita, 1987; Kilcher and Nash, 2010]. However, quantifying frontal turbulent mixing rates as a function of time has been much more challenging. To date, geophysical scale observations of near-frontal  $\varepsilon$  have been in one of two categories: Either spatially well-resolved, but for a snapshot in time or spatially poorly resolved (length scales much larger that  $L_G$ ) but over long time periods. The research of Kilcher & Nash [2010] in the Columbia River plume has come closest to attaining satisfactory temporal and spatial resolution by showing the evolution of mixing near the front from five transects over a 15-h period. However, due to the large scale of the plume, microstructure profiles were at least 500 m apart and  $\epsilon$  values above 5 m depth were excluded due to freefalling profiler limitations, excluding a very active portion of the plume.

Additionally, the frontal structure may be affected by the orientation of the bulk flow relative to the front, such that a lateral front can be defined where the bulk flow is in the along-front direction, with a leading-edge front in locations where flow is primarily normal to the advancing front. The difference in flow structure may play a key role in delivering freshwater to the front and maintaining the structure of the front as the plume ages, affecting velocity and density profiles and potentially the turbulent environment present at the frontal head. Ultimately, a plume front may have sections along its length characterized as lateral or leading-edge, and these may transition over the course of a tidal cycle, due to ambient currents, wind velocities, and proximity to the near-field buoyant jet. There has been limited research comparing

these two types of plume fronts in terms of their structure and mixing, but doing so might better constrain the contribution of frontal mixing to the total dilution of estuarine discharge.

Lastly, there has been limited intercomparison of river plume turbulence data from different estuarine systems. Such an analysis could reveal correlations between plume parameters, and the cross-front distribution and magnitude of  $\epsilon$ .

Section 2 of this manuscript introduces the observational program and the underlying environmental conditions. In Section 3, we show how frontal structure and mixing intensity compare between two distinct frontal regions, characterized by both flow orientation and distance from the river mouth. In Section 4, we identify the generation and decay characteristics of turbulence in the near-frontal region, and present side by side comparisons between the TKE dissipation rates that were derived from turbulent microstructure data and from overturn scales. We also compile data from four previous plume studies and present a method for nondimensionalizing dissipation rates in an effort to better assess frontal mixing over a wide range of plume sizes. Results are summarized in Section 5.

#### 2. Observational program

The study was conducted on the afternoon of October 24, 2019, offshore of the Connecticut River mouth, in eastern Long Island Sound (LIS) on the East Coast of the United States, as shown in Fig. 2. The brackish and high sediment water of the Connecticut River estuary discharges to the south into LIS forming a thin buoyant plume, the location and shape of which are primarily dictated by the magnitude and direction of LIS tidal currents. During ebb, LIS flows to the east, while at flood, current direction reverses. A phase lag between the beginning of the flood tide and the reversal of estuarine discharge [Whitney et al., 2021] causes the river mouth to continue ejecting buoyant estuarine water at least 4 h after low tide. This study was focused on a time-period starting at low tide and ending around peak flood flow approximately 3.5 h later.

#### 2.1. The T-REMUS

The UMass Dartmouth T-REMUS, a custom designed Hydroid Inc. AUV, was the main data collection platform. Its leading edge is equipped with a Rockland Scientific Micro ASTP microstructure measurement sensor and a Sea-Bird 49 FastCAT CTD sensor that sampled at 500 Hz and 16 Hz respectively. Upward and downward 1.2 MHz RID Acoustic Doppler Current Profilers (ADCP) sampled velocity and echo amplitude at 1.25 Hz and averaged data over 25 cm vertical bins. The T-REMUS was programmed to navigate exclusively in the reference frame of a Hydroid Inc. GatewayBuoy, which was tethered to the University of Connecticut support vessel. The vessel maintained a constant distance west of the front while the T-REMUS navigated constant-depth outbound and inbound legs using the vessel attached buoy as a target navigation beacon. This AUV was previously used in river plume environments in research described by MacDonald et al. [2007] and Mac-Donald et al. [2013] which demonstrated its capability of making accurate microstructure measurements of turbulent mixing in the energetic environment of river plumes, particularly through the plume interior. During T-REMUS missions, a DJI Phantom 4 pro UAV was launched off the support vessel and was flown directly above the plume front while maintaining GPS-equipped surface drifters in the field of view. The recorded footage gave helpful insight into the overall front behavior and its interaction with LIS water.

Three distinct AUV missions were conducted which are labeled as Run 1, Run 2, and Run 3 in Fig. 2a. Details of transects within each Run are shown in Table 1. Run 1 was located approximately 700 m south of the jetties and started 4.7 h after High Water (HW) at a time when the eastward flowing ebb was decelerating. At that time near the river mouth, the plume was attached to the west river jetty and flowed

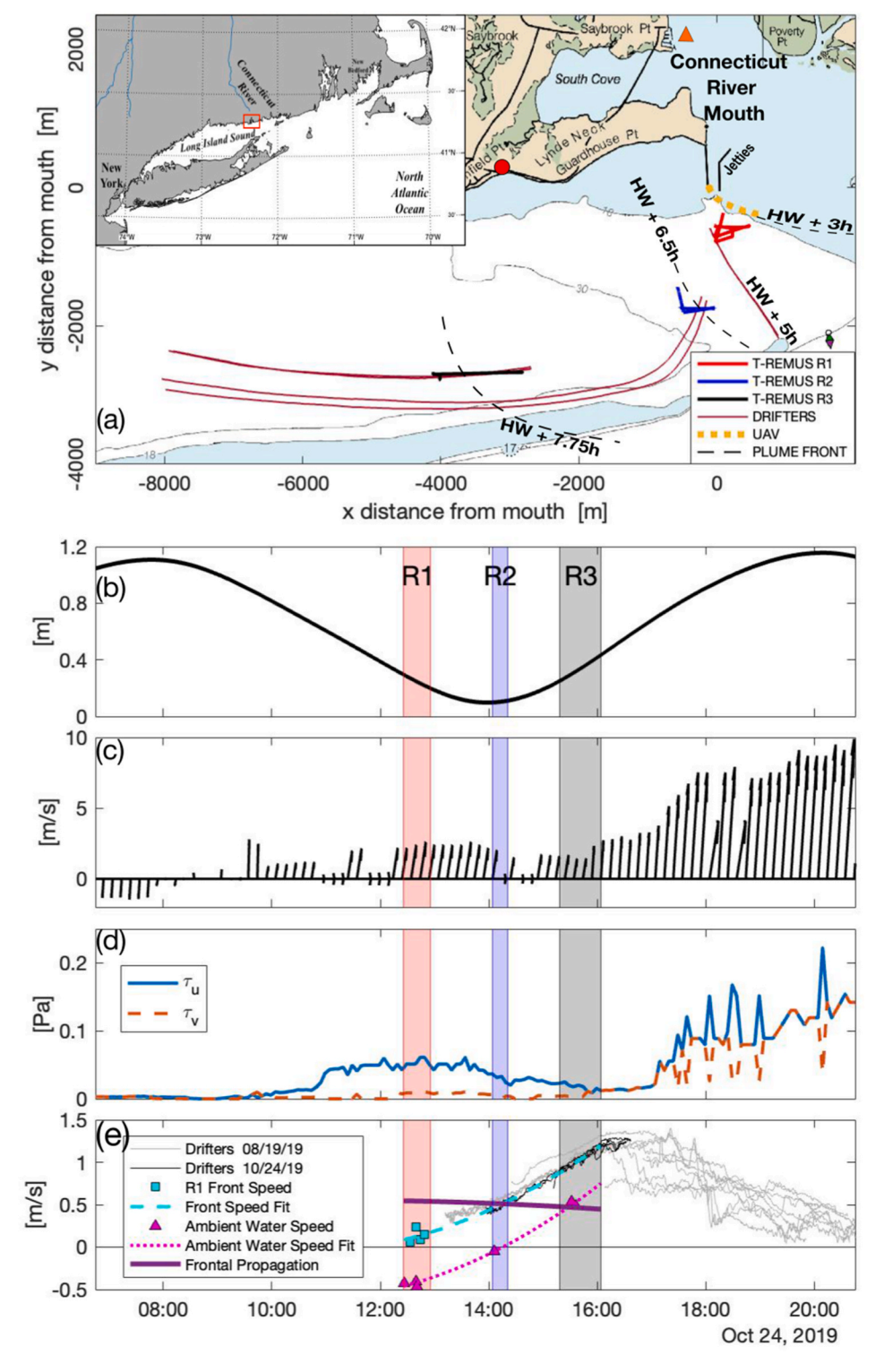


Fig. 2. (a) Locations of three T-REMUS missions labeled as R1, R2, and R3 are seen as bold lines. Drifter tracks are annotated with thin curves. Unmanned Aerial Vehicle track while flying above the plume front is seen as the dotted yellow line. Dashed black curves indicate the location and shape of the front at four times referenced to High Water. Red circle indicates meteorological station location. Orange triangle indicates location where CO-OPS tidal predictions were made. The axis origin is set at the jetties entrance and chart bathymetry is in ft. (b) Tidal height calculated at the location of the orange triangle, (c) wind direction and speed, (d) along-coast (solid) and across-coast (dashed) wind stress. (e) Drifter velocities while trapped at the convergence zone of the plume flood front on 10/24/19 (black) and on 08/19/19 (grey) after aligning to High Water. Subtracting ambient water velocities from drifter velocities gives the frontal propagation speed in reference to a motionless ambient layer (thick curve). Durations of Runs 1, 2, and 3 are shaded in red, blue, and grey respectively. (For interpretation of the references to color in this figure legend, the reader is referred to the Web version of this article.)

towards the southeast and east creating a visible lateral front along its southern boundary. The morphology of this front in time and space was first described by Garvine, 1974 and Garvine & Monk [1974], who identified its surface expression by a color change no wider than 0.5 m that coincided with foam and other floating debris. The ebb flow diminished during the time between Run 1 and Run 2, allowing ejected estuarine water to expand the plume southward and thereby causing the jetty-attached lateral front to slowly swing towards the southwest. While the estuary continued to discharge and as LIS flood currents began to

accelerate westward, the plume was stretched towards the west. This transformed the lateral front sampled in Run 1 into a leading-edge front. Between Runs 2 and 3, plume streamlines experienced a sharp west turn shown in the drifter tracks (red lines) of Fig. 2a. Run 2 provided limited data through the front, as the orientation of the mission resulted in the vehicle falling behind the frontal zone. The vehicle was retrieved and reset into position for Run 3, which was located approximately 5 km SW of the jetties and started 7.5 h after HW during which time the strongest flood currents were observed ( $\sim$ 0.8 m/s).

Table 1
Summary of t-REMUS Runs and transects.

TransectID	Time in EDT [hh:mm:ss]	Direction of Travel Relative to Plume	Cross-Front Distance Travelled [m]	Mean Transect Depth [m]	Mean T-REMUS Velocity [m/s]	Mean Sampling Angle [deg]	Mean Front Bearing [deg]
Run 1A	12:26:33 - 12:31:10	Inbound	418	4.2	1.6	-1.6	153
Run 1B	12:32:31 - 12:29:37	Outbound	416	1.2	1.1	-0.44	153
Run 1C	12:39:48 - 12:41:55	Inbound	129	1.3	1.2	044	153
Run 1D	12:45:15 - 12:48:38	Outbound	213	1.2	1.2	-0.48	153
Run 1E	12:48:46 - 12:54:56	Inbound	346	1.3	1.2	-0.46	154
Run 2A	14:05:06 - 14:11:41	Inbound	497	4.0	1.1	-1.36	154
Run 3B	15:18:38 - 15:23:56	Inbound	382	4.0	0.7	-2.00	167
Run 3C	15:24:33 – 15:33:53	Outbound	525	1.2	2.2	-0.47	167
Run 3D	15:34:10 – 16:03: 52	Inbound	1321	0.7	0.1	-0.69	170

Each T-REMUS Run was segmented alphabetically into transects of relatively constant depth and heading. Five front-crossing transects were made during Run 1, one during Run 2, and three during Run 3. Frontal crossings were determined as the location with the highest rate of change in salinity. Drifter positions were used to find the front's speed and bearing which were then used to calculate the vehicle's across and along-front distance to the propagating front. In the following figures where the x-axis is distance to the front, negative x values always represent conditions in ambient LIS water, with  $\mathbf{x}=0$  representing the frontal crossing. Note that Run 1 transects were oriented mostly perpendicular to plume streamlines generating cross-sectional views of the plume whereas in Run 3 transects were oriented parallel to plume streamlines generating views along the plume main axis.

The shear probes of the microstructure sensor output values that are proportional to the rate of change of cross-stream velocity:  $\frac{\partial w}{\partial x}$  and  $\frac{\partial v}{\partial x}$ , where w is the vertical velocity, v the lateral velocity, and x the direction of travel [RGL Consulting Ltd., 2003]. The rate of dissipation of TKE under the assumption of isotropic and homogeneous turbulence was calculated with:

 $\varepsilon=\frac{15}{2}\nu\overline{\left(\frac{\partial v}{\partial x}\right)^2}=\frac{15}{2}\nu\overline{\left(\frac{\partial w}{\partial x}\right)^2}=\frac{15}{2}\nu\int_0^\infty \Psi(\kappa)\,d\kappa$  The overbars denote spatial averaging,  $\nu$  is the kinematic viscosity,  $\nu$  and w the turbulent velocity fluctuations,  $\Psi$  the velocity shear spectrum, and k the wavenumber [*Lueck*, 2016]. Using the sensor's accelerometer data, vehicle motion and vibration contamination was removed from the  $\varepsilon$  estimates according to the procedures presented by [Levine et al., 2009; Goodman et al., 2006].

## 2.2. Environmental conditions

The three-day mean river discharge prior to the field program was 388  $m^3/s$  measured at the Thompsonville, CT USGS station which was below the long-term annual mean of 491  $m^3/s$  and well below the mean freshet value of 1133  $m^3/s$  which occurs in late spring. The field program was conducted four days after a neap tide with tidal prediction data from the CO-OPS Saybrook Point Station (ID: 8,462,752) showing an amplitude of 0.97 m (Fig. 2b). Southwest winds prevailed throughout the field study. Wind speed magnitudes ranged from 5 m/s during Run 1-4 m/s and 3 m/s during Runs 2 and 3 respectively (Fig. 2c). The along and across-shore components of wind stress were calculated using the equation  $T = C_D \rho_a U^2$ , where  $C_D$  is a dimensionless drag coefficient equal to  $1.2\times 10^{-3}$  for velocities ranging from 4 to 11 m/s [Large and Pond, 1981],  $\rho_a$  the air density, and U the along or across shore wind speeds. Across-shore wind stress was nearly zero throughout the field study, while along-shore wind stress ranged from 0.05 Pa during Run 1 to 0.025 Pa during Run 3 (Fig. 2d). Meteorological data came from a private Weather Underground, Inc. Station (ID: KCTOLDSA23) located near the coast on the Lynde Neck peninsula.

For each transect, the ambient across and along-front water speeds were estimated by averaging ADCP data within the cross-front distance of -50~m to -10~m and for all depths. Mean ambient water velocities ranged from 0.5 m/s eastward to 0.7 m/s westward while the front speed

over ground ranged from 0.1 to 1.15 m/s. The difference yields a frontal propagation speed in the reference frame of the ambient LIS water that was approximately constant around 0.5 m/s for all Runs. A field program on August 19, 2019, provided supplemental frontal speed data from surface drifters that were deployed along the front. After adjusting times to HW, August 19 drifter velocities match well with those deployed on October 24 even though the mean three-day discharge was 3.5 times lower ( $10.8m^3/s$ ) and the tidal range 0.08 m smaller (0.89 m). Despite the differences in environmental conditions, the trajectory of drifters during both releases were in good agreement (Fig. 2e).

#### 3. Front anatomy

This section investigates how density anomaly and TKE dissipation were spatially distributed and how they evolved with time. We incorporate vehicle attitude data, such as deviation of speed and depth from target values, and georectified UAV imagery to better understand the dynamics and structure of the plume front. ADCP cross-sections of velocity and backscatter anomaly provide detailed views of the evolving front head and plume body.

# 3.1. Cross-front transects

Fig. 3 shows (a) depth, (b)  $\sigma_{\theta}$ , and (c)  $\varepsilon$  for all T-REMUS shallow transects as a function of distance to the plume front and captures how conditions in the plume interior differ from those at the frontal region. Turbulence, as indicated by  $\varepsilon$ , generally peaks in the downwelling zone immediately behind the front, with  $\varepsilon$  decreasing with distance into the plume interior. This trend is also corroborated by the spatial-temporal variability of  $\sigma_{\theta}$  along each transect, as indicated in Fig. 3b. The density difference between LIS and plume waters ranged from 8 to 13 kg/  $m^3$ . Throughout the observational program, the horizontal density gradient at the front was consistently sharp (O (1 m) wide) indicating that highly buoyant surface water was continuously replenished. Associated with this sharp density gradient,  $\varepsilon$  increased by three orders of magnitude within 4.5 m while crossing from LIS to plume waters, illustrating how narrow the band of active turbulence can be and why it has been so challenging to measure frontal mixing. At the front, the T-REMUS was observed to abruptly deflect and lose altitude at every crossing, regardless of initial transect depth or travel direction. The vehicle was forced downward by as much as 0.75 m, as shown in Fig. 3a, while position data indicate it was also accelerated towards the front and to the south along the front before adjusting back to the programed depth and heading.

Two distinct frontal zones are apparent in the data of Fig. 3. From 0 to O (10) m (identified as "Z1" in Fig. 3), highly buoyant surface water was detected between 0.75 m and 2 m depth which further suggests a strong downwelling pattern from the plume surface towards the front head. In this downwelling zone  $\sigma_{\theta}$  was highly variable but trended to higher values with distance away from the front. The maximum  $\varepsilon$  values were observed in this downwelling zone (of order  $10^{-4}$  m<sup>2</sup>/s<sup>3</sup> to  $10^{-3}$  m<sup>2</sup>/s<sup>3</sup>) approximately 2.5 m behind the front. During the time of Run 3,

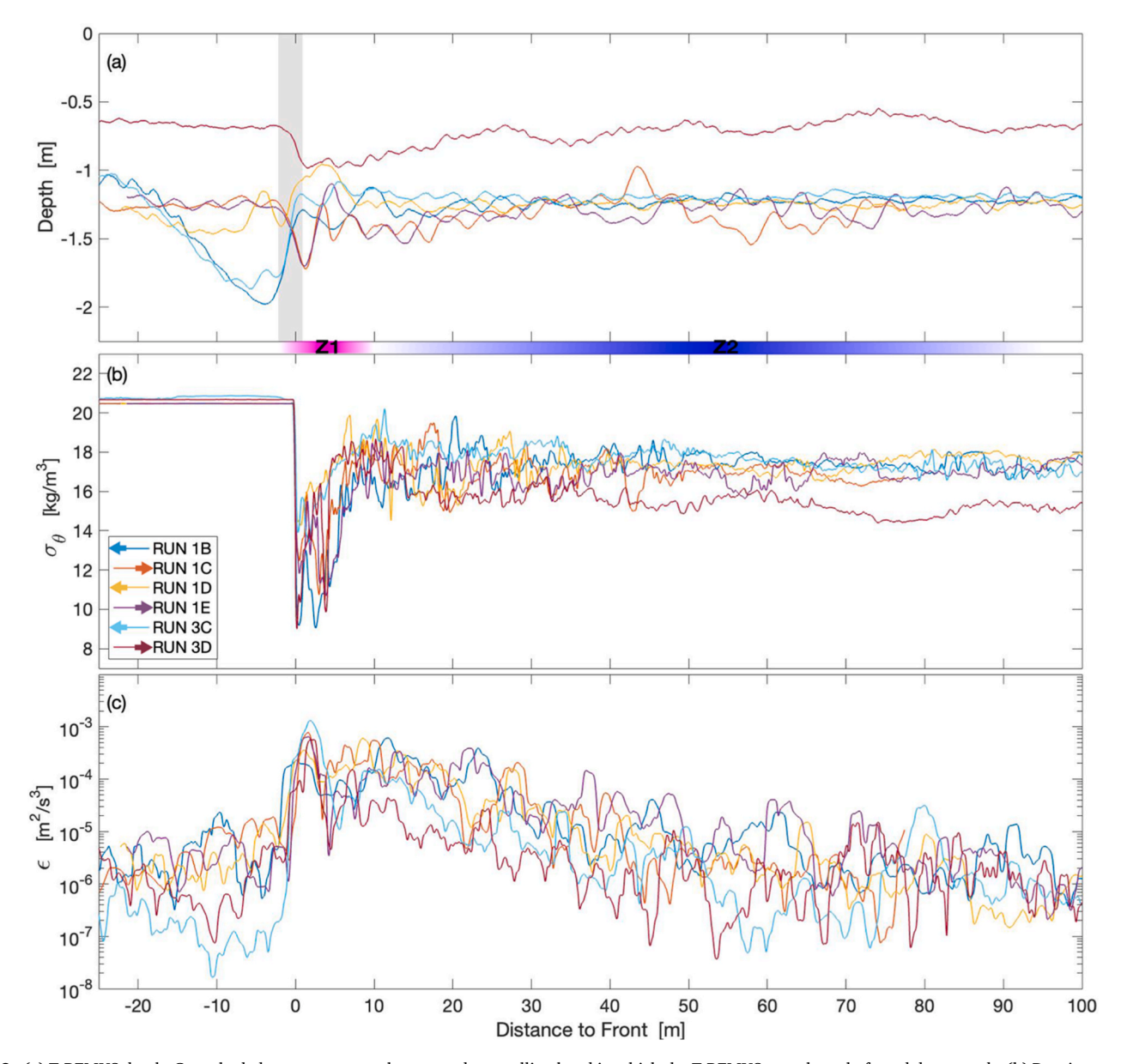


Fig. 3. (a) T-REMUS depth. Grey shaded area represents the strong downwelling band in which the T-REMUS was abruptly forced downwards. (b) Density anomaly, and (c) TKE dissipation rate. Arrows in legend indicate the direction of T-REMUS travel during each transect. Horizontal color bar between (a) and (b) indicates the approximate cross-front width of Z1: downwelling zone, and Z2: trailing frontal zone. (For interpretation of the references to color in this figure legend, the reader is referred to the Web version of this article.)

this zone had the same width as the band of foam seen in UAV images. Beyond O (10) m to O (100) m we observe the trailing frontal zone ("Z2" in Fig. 3). In this range,  $\epsilon$  values gradually reduce to interior plume levels with increasing distance from the front, again corroborated by decreasing  $\sigma_{\theta}$  variance. Beyond O (100) m (not shown in Fig. 3) the stable interior region of the plume is characterized by stable stratification and  $\epsilon$  values comparable to those observed in the ambient LIS.

Overall, in all Runs these three zones were observed to maintain their width and distance behind the front, as well as, density and  $\epsilon$  characteristics which suggest that they form independent of the front's angle to the direction of plume propagation. For all Runs TKE dissipation was of order  $10^{-3}~\text{m}^2/\text{s}^3$  immediately behind the front and decayed to  $10^{-6}~\text{m}^2/\text{s}^3$  approximately 100 m into the plume. This decay length scale is similar to that observed by <code>O'Donnell</code> et al. [2008]. Beyond 100 m from the front,  $\epsilon$  was relatively constant ranging between  $10^{-7}$  and  $10^{-6}~\text{m}^2/\text{s}^3$ .

## 3.2. Vertical profiles

Profiles of  $\sigma_{\theta}$ ,  $\varepsilon$ , and horizontal velocity magnitude were assembled by averaging equivalent depth values over five different windows in the cross-front direction. The column of plots (a, e, and i) on the far-left side of Fig. 4 represent LIS ambient waters, while the right-most column (plots d, h, and l) show conditions in the plume interior. LIS water was well-mixed throughout the ambient water column and showed no indication of residual fresh water at the surface from previous tidal pulses (Fig. 4a). This absence was likely due to strong tidal mixing in LIS (Simpson and Britter, 1979; Spicer et al., 2021) and lower than average discharge conditions. TKE dissipation in LIS was of order  $10^{-6}$  m<sup>2</sup>/s<sup>3</sup> from the bottom to 1 m depth and increased to  $10^{-4}$  m<sup>2</sup>/s<sup>3</sup> near the surface (Fig. 4e).

Ambient waters during Run 1 were significantly more turbulent than in Run 3, which was consistent with wind stress decreasing by more than 50%. The 10 m wide downwelling zone immediately behind the front

(Fig. 4b, f, j) was comprised of three distinct layers. The upper well mixed layer, bounded between 0 and 0.75 m depth, had a low  $\sigma_{\theta}$  of minimal variability at around 8 kg/  $m^3$ . The intermediate layer was between 0.75 and 2.25 m depth and had great variability in  $\sigma_{\theta}$  which persisted for all Runs. This layer represents the turbulent core of the frontal head. It is consistently associated with some of the highest  $\varepsilon$  values, reaching up to  $10^{-3}$  m<sup>2</sup>/s<sup>3</sup>. The third layer was below 2.25 m depth and had the same dissipation and  $\sigma_{\theta}$  characteristics as the ambient water. The sharp boundary between the top buoyant layer and the turbulent core and between the turbulent core and the ambient water gradually eroded for consecutive sections behind the downwelling zone (Fig. 4c and d).

The plume shear layer of Run 1 is seen above 1.5 m depth, below which velocities are mostly uniform (red in Fig. 4j, k, l). In Run 3 velocities decrease more gradually with depth indicating a thickening of the shear layer and diffusion of momentum downwards (black in Fig. 4j, k, l). It should be noted that velocity plotted in Fig. 4(i–l) represent the magnitude of the horizontal velocity. In Run 1, the velocity vector is

directed primarily in an along front direction, given the lateral orientation of the front. In Runs 2 and 3, the direction is primarily cross-front.

The presence of a homogenous 0.75 m thick surface layer of very low density water ( $\sigma_{\theta} \sim 8 \text{ kg/m}^3$ ) at the front (Fig. 4b) was surprising to see given that the front at that time was 5 km away from the river jetties. Unfortunately, we do not have additional near-surface data to confirm the mechanism that maintains this highly buoyant fluid at the front, however it is possible that a very thin even more buoyant overflow layer, as seen in the schematic of Fig. 1b, replenishes this fluid.

#### 3.3. ADCP cross-sections

The two-dimensional distribution of backscatter anomaly and velocity is displayed in Fig. 5 for transects 1 A, 2 A and 3D. ADCP data from the T-REMUS was carefully post processed using a bin-mapping technique to account for pitch and roll of the vehicle (eg. MacDonald et al., 2007), and vehicle motion (in x, y, and z) was subtracted from the resulting velocity estimates. Although it is conventional to analyze

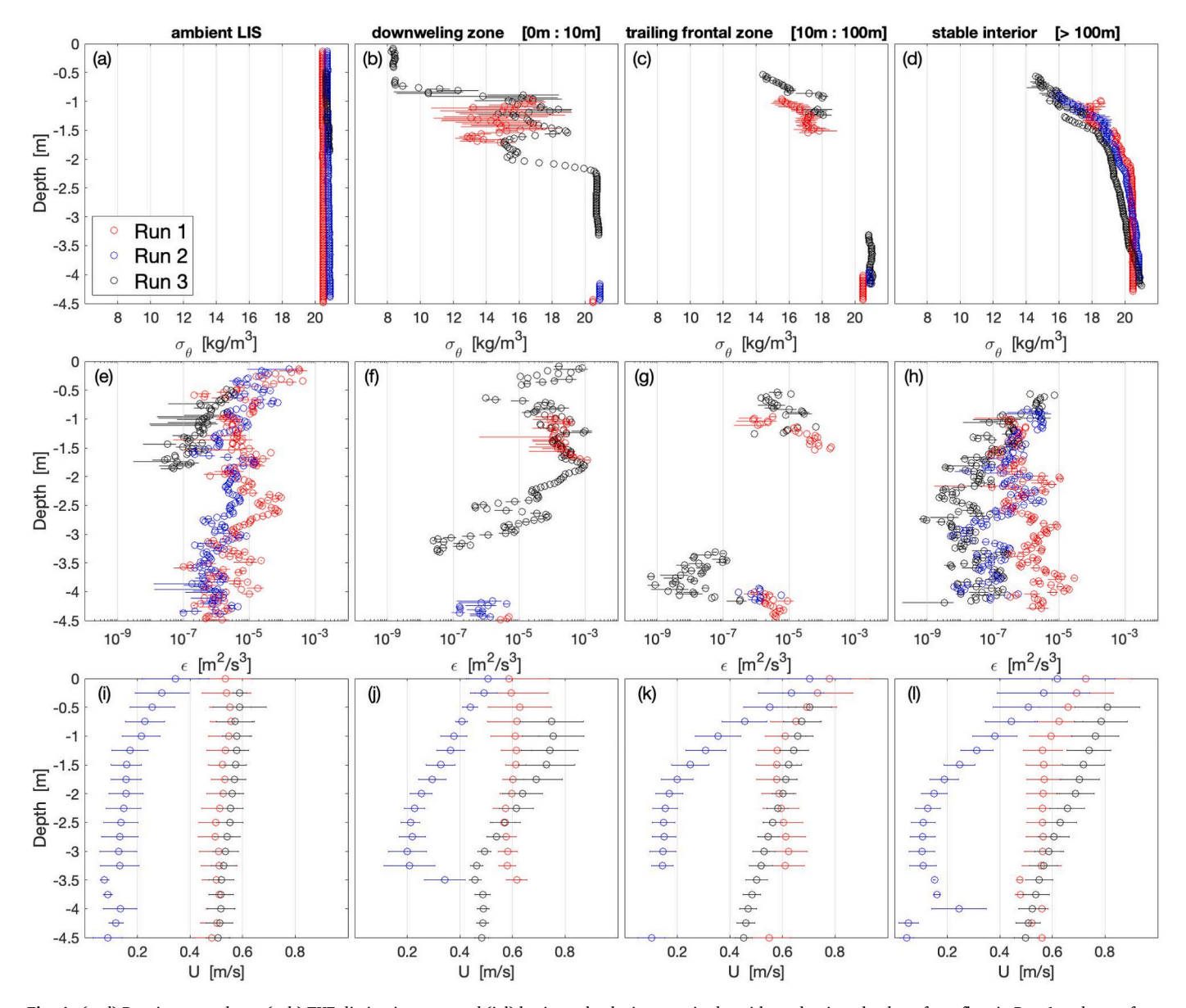


Fig. 4. (a–d) Density anomaly  $\sigma_{\theta}$ , (e–h) TKE dissipation rate, and (i–l) horizontal velocity magnitude, with predominantly along-front flow in Run 1 and cross-front flow in Run 3, as a function of depth averaged over four across-front zones. In all panels, Run 1 seen in red, Run 2 in blue, and Run 3 in black. Circles indicate the mean values while horizontal lines are 95% CIs. Circles with no error bars signify a sample size of one. (For interpretation of the references to color in this figure legend, the reader is referred to the Web version of this article.)

frontal processes in a reference frame moving with the front, in this manuscript we plot data relative to the ambient flow in Long Island Sound ahead of the front so that frontal processes can be better visualized and not obscured by the strong tidal flows present ahead of, and beneath, the plume. High backscatter values signify areas with high concentrations of bubbles and debris, typically observed in the plume, while substantially lower values were typically observed in ambient LIS waters. The location and shape of the front head is clearly visible in all transects. It is characterized by high levels of backscatter in its interior, a sharp outline on the leading edge, and a gradual transition to lower backscatter values behind it. These observations accord with the cross-front distributions of density and dissipation through the frontal head region. Velocity vectors indicating convergence and downwelling also match very well with the outline of the front head. In particular, these observations, together with the evidence of buoyant surface water from 0.75 to 2 m depth near the front, are evidence that streamlines near the plume surface curved downwards in the immediate vicinity of the front, while successively deeper streamlines curved downwards at an increasing distance from the front. This flow pattern is similar to that drawn in the schematic of Luketina and Imberger, 1987 in Fig. 1b.

Similarly, the frontal head of transect 1 A presents strong evidence of a rotating cell which has a width of 20 m and extends from the surface down to 6.25 m depth. This rotor is an order of magnitude narrower than what Luketina & Imberger [1987] observed at the Koombana Bay outflow but of similar depth ( $\sim$ 4 m). Such a cell is not clearly evident in 3D, although strong downwelling and subduction of ambient water that reaches the seafloor is observed.

In transect 1 A downward velocities had a maximum of 0.15 m/s at 1.75 m depth, but in 3D they were uniform throughout the water column at 0.06 m/s. In general, with increasing distance from the jetties, the decrease in downwelling velocities was substantial and the depth at which maximum values occurred increased. These observations are consistent with O'Donnell [1997] who also took measurements across the Connecticut River plume front in approximately the same location as our transects in Run 1, and estimated downwelling velocities of order 0.1 m/s using continuity with no along-front divergence. Since transect

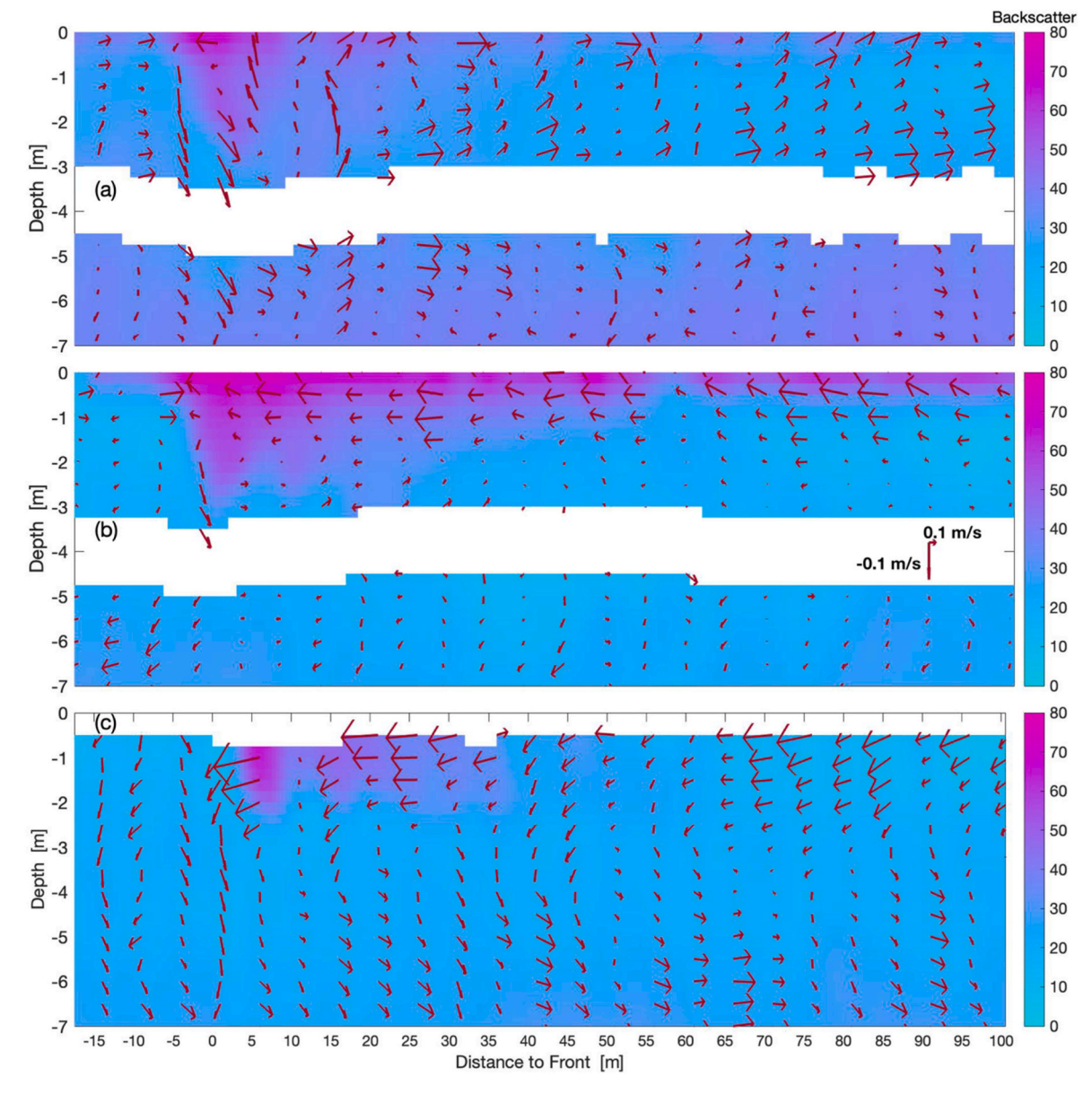


Fig. 5. Cross-front and vertical velocity field in the reference frame of ambient water ahead of the front superimposed over backscatter anomaly. Areas seen in magenta represent regions high in debris and bubbles. (a) Transect 1 A, (b) Transect 2 A, (c) Transect 3D. White areas are due to blanking distance of the upward and downward looking ADCPs.

1 A crossed a lateral front, that was slowly propagating westward, there was no distinct surface layer with overtaking velocities that fed into the frontal region. The front head was most likely energized by the ebbing (eastward directed) ambient LIS, which was forced to dive under the buoyant southward jet of estuarine water. The subduction of ambient water, combined with a steep barotropic gradient, may be the mechanisms that maintained the rotating cell that was seen at the front head.

#### 3.4. Summary of near-frontal structure

Fig. 6a presents an aerial view of the frontal region, taken from the UAV, while 6 b highlights the structural features in the plume near-frontal region. In many respects, the overarching frontal structure of the Connecticut River plume resembles that presented in previous laboratory and field studies, as seen in Fig. 1. For example, in both figures, the relative shapes and velocity fields of the frontal head are analogous to one-another. However, our sampling methodology which allows for uniquely high levels of detail, enhances this view by combining velocity, turbulent microstructure, and density measurements in one high-resolution schematic.

#### 4. River plume turbulence

#### 4.1. Turbulence scaling and isotropy

In this section, we describe the generation and decay characteristics of turbulence in the context of nondimensional numbers and length scales. Fig. 7a summarizes these findings and shows  $\varepsilon$  values averaged over 1 m cross-front bins using all available shallow T-REMUS transects of Run 1 (red circles) and Run 3 (black triangles).

Fitting regressions of the form:  $\varepsilon(x)=\varepsilon_o \exp(-x/L_G)$  to the observed TKE dissipation rates gave the decay scale  $L_G$  which describes the rate at which turbulence decays as a function of distance away from the front [O'Donnell et al., 2008]. Fig. 7a shows these fitted lines for Runs 1 and 3 and suggest a slightly higher spatial decay rate during Run 3 than Run 1. Data from 0 to 100 m were used to determine the appropriate fit in both cases

As discussed in Section 1, prior research [e.g., *Iven and Imberger*, 1983] has identified two  $Re_b$  thresholds that help classify turbulence as anisotropic, transitioning, and isotropic.

For  $Re_b < 21$  turbulence ceases to be isotropic and active as a result of being suppressed by vertical density gradients, for  $Re_b$  values between 21 and 464 turbulence is transitioning to isotropy, and for  $Re_b > 464$  turbulence is strong and fully isotropic. Fig. 7a also shows the two  $Re_b$  thresholds, rearranged in terms of  $\varepsilon$ , as the lines labeled  $\varepsilon = 21\nu N^2$  and  $\varepsilon = 464\nu N^2$ . Turbulence is strong and fully isotropic within 5 m behind the front, which approximately corresponds to the cross-front width of the turbulent core. From 5 m to about 55 m, turbulence is well developed but becomes increasingly altered by the stratification, which introduces anisotropy [Garvine and Monk, 1974]. Beyond 70 m, turbulence is consistently suppressed by strong density gradients.

Itsweire et al. [1993] observed in laboratory grid experiments that the vertical buoyancy flux (B) was greatly diminished after 5 buoyancy periods from the generation location. With a mean flow velocity U, the distance to which the instabilities were advected before ceasing to mix surrounding fluid was measured as:  $L_I = \frac{SU}{N}$ . If we assume that analogies can be drawn between the grid experiments and river plume fronts, then  $L_I$  can be used to estimate how far turbulent patches might have been advected from the turbulent core towards the wake region. To estimate  $L_I$ , the frontal propagation speed, described in section 2.2, was averaged for each Run and was substituted for U as a representative velocity. N was calculated using sorted density micro-profiles along T-REMUS transects, a method similar to that described in section 4.2, but in this case analyzed between adjacent data points. Fig. 7b shows that  $L_I$  increases from 3 to approximately 8 m when transiting from 0 to 55 m in

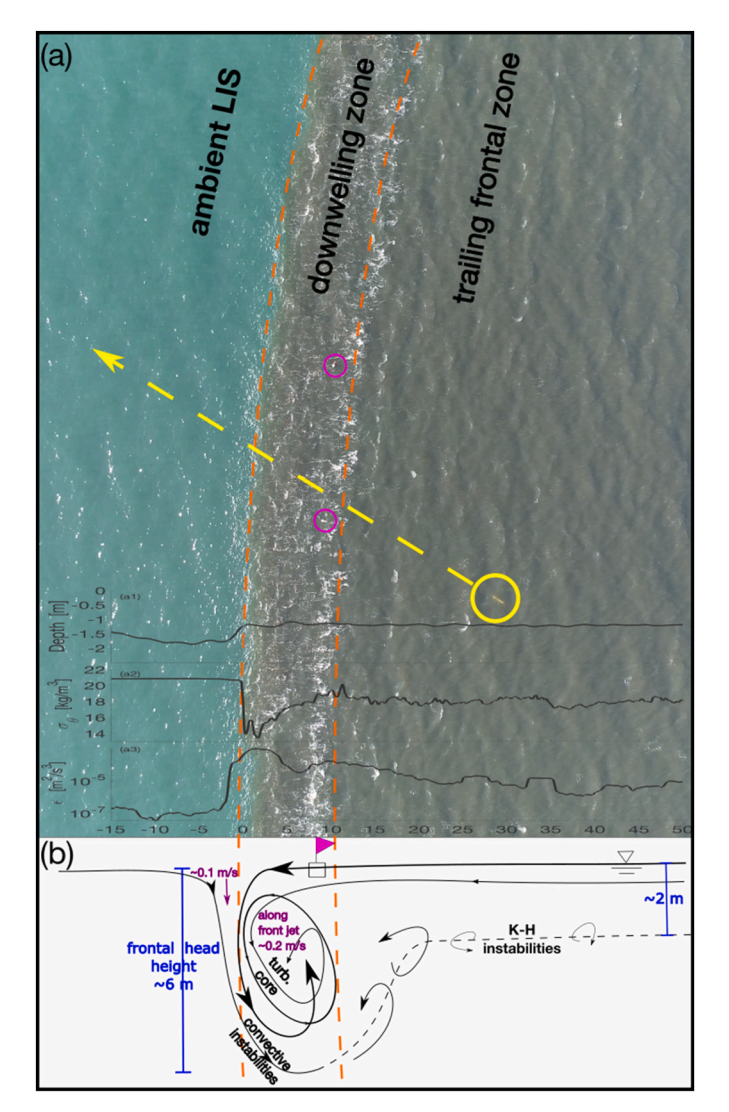


Fig. 6. (a) Plan view of plume frontal region during transect 3C. Image was georectified using UAV metadata and ArcGIS Pro. Dashed vertical curves segment the plume in two distinct regions. Data from transect 3C showing T-REMUS depth in (a1),  $\sigma_{\theta}$  in (a2), and  $\varepsilon$  in (a3). Magenta circles highlight the locations of two surface drifters. The yellow arrow signifies the T-REMUS transect, while the yellow circle highlights its position. The width of the downwelling zone ( $\sim$ 10 m) corelates well with the band of bubbles and detritus. (b) Schematic of plume side view with the vertical direction representing depth and the horizontal direction, distance to the front. (For interpretation of the references to color in this figure legend, the reader is referred to the Web version of this article.)

cross-front distance. In the 0–25 m range, which bounds the downwelling and mixing zones,  $L_{\rm I}$  is approximately equal to 4 m which implies that advection of turbulence should be minimal with the turbulent core having a relatively short wake.

# 4.2. Comparing TKE dissipation rates derived from microstructure and overturn scales

Although the T-REMUS was programmed to run transects at a constant depth, it fluctuated about the target depth with amplitudes as large as 0.45 m and a median sampling angle of 3°. These fluctuations generated mostly monotonic CTD transect segments which were isolated and analyzed using an algorithm similar to that developed by *Ferron* et al. [1998] and *MacDonald* et al. [2013] for calculating overturn scales,  $L_T$ , as well as local estimates of the buoyancy frequency,  $N^2$ . It should be

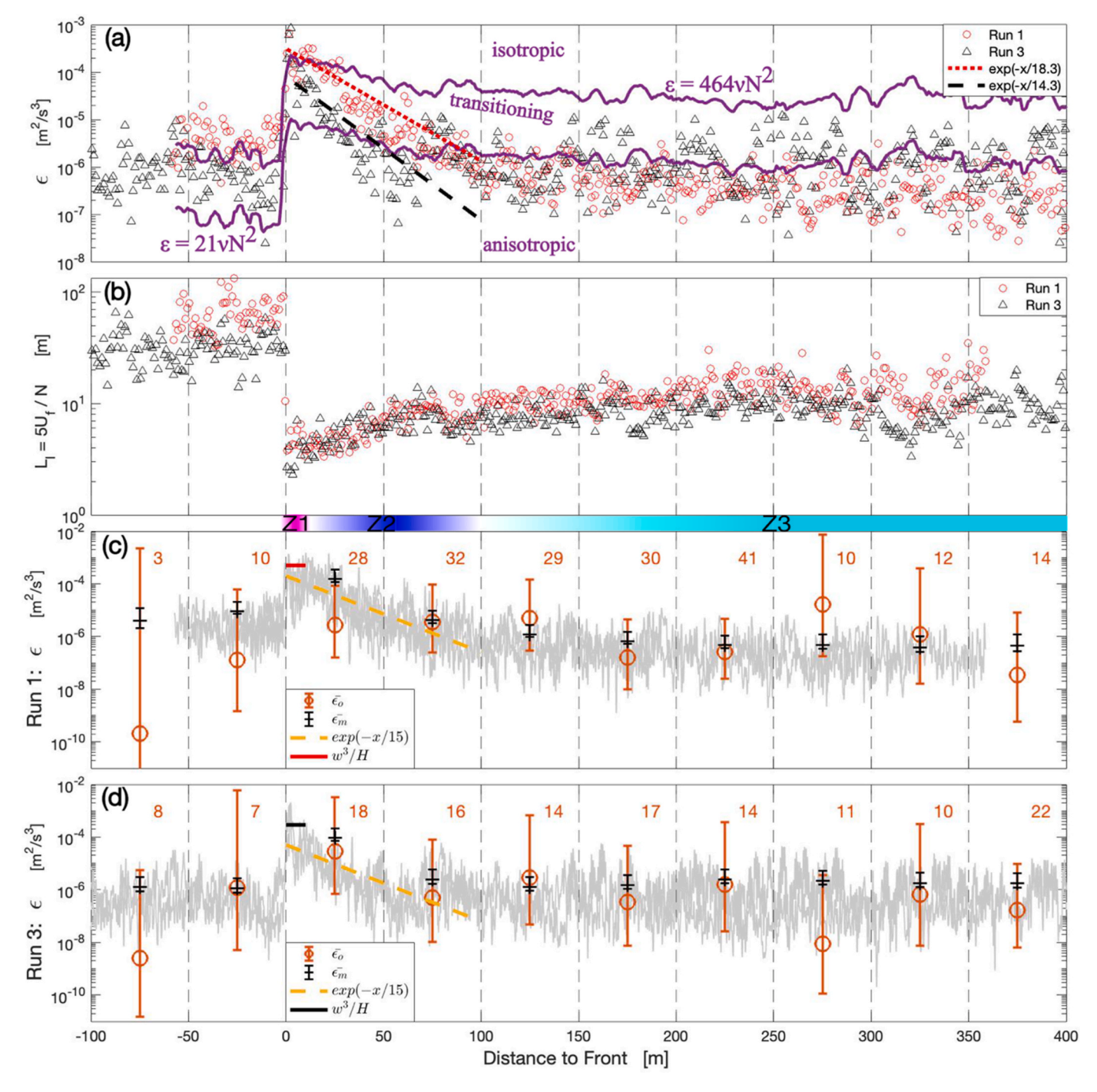


Fig. 7. (a) TKE dissipation rate averaged over 1 m cross-front bins using all available shallow T-REMUS transects of Run 1 (red circles) and Run 3 (black triangles). Red and black dashed lines are fitted regressions of the form:  $ε(x) = ε_o \exp(-x/L_G)$  for Run 1 and Run 3 data respectively. The two purple curves show the upper and lower thresholds of  $Re_b$ . (b) Itsweire length scale as a function of distance to front. (c, d) Lognormally distributed volumetric means of ε from overturn scales,  $\overline{ε_o}$ , (red circles) and from microstructure,  $\overline{ε_m}$  (black dashes), averaged over 50 m cross-front bins. Grey curves are the non-averaged microstructure ε from shallow transects. Transects 1 B, 1C, 1D, and 1 E, were used for the distribution mean estimates of (c), and 3C, 3D, were used for (d). Dashed yellow lines show the exponential decay exp (-x/15) observed by O'Donnell et al., [2008] in the Connecticut River plume. The standard errors at 90% confidence limits are plotted, while the adjacent numbers signify the overturn ensemble sizes within each cross-front bin. Red and black horizontal line segments in (c) and (d) respectively, show the magnitude of scaled ε. The horizontal color bar between (b) and (c) indicates the approximate cross-front width of Z1: downwelling zone, Z2: trailing frontal zone, and Z3: stable plume interior. (For interpretation of the references to color in this figure legend, the reader is referred to the Web version of this article.)

mentioned that the method utilized relied on a comparison of observed and sorted density profiles, to identify overturns, and any regions with overturns that were not completely resolved within the vertical excursion were removed from the analysis.  $N^2$  values were calculated for each overturn using the sorted profile, so that estimates were not impacted by regions of unstable data. The method was used successfully for resolving

overturns in longer yo-yo profiles conducted by the same T-REMUS vehicle at similar angels of attack in MacDonald et al., [2013], and comparison of yo profile results to subsequent constant depth data in a related study of the Connecticut (not shown) suggest the data collected over the small scale vertical excursions is consistent with larger scale estimates. Using equation (2) with the observed overturn and buoyancy

frequency data, and setting  $\alpha=1$ , the TKE dissipation from overturns  $(\varepsilon_O)$  was estimated.  $\varepsilon_O$  values from successive 50 m cross-front bins were grouped to calculate averages that assumed a lognormal distribution. A key advantage of this averaging method is that it accounts for the tail end of the lognormal distribution, where the largest overturns, which produce the highest  $\varepsilon_O$  values, may not be sufficiently sampled by the T-REMUS since they are short-lived and occur more rarely [MacDonald et al. 2013]. The same methods were applied to the microstructure derived TKE dissipation rates  $(\varepsilon_m)$ . The confidence limits at 90% shown in Figure 12 of MacDonald et al. [2013] were applied to our data. This way, by knowing the ensemble size associated with every 50 m cross-front bin, confidence intervals encompassing the anticipated mean could be calculated.

Fig. 7c and d shows the lognormally distributed means of TKE dissipation from overturn scales,  $\overline{\epsilon_o}$ , (red circles) and from microstructure,  $\overline{\epsilon_m}$ , (black dashes), which are plotted over the raw high-frequency microstructure data (grey lines) as a function of distance to the front. The overturn ensemble size in each case, generally ranging from 10 to 30, is displayed next to the confidence limits for each 50 m cross-front bin. The microstructure sample size in each bin ranged between 1000 and 2000, which resulted in much tighter confidence limits.

With data from Run 3, the two independent methods for estimating TKE dissipation produced comparable results (Fig. 7d) even though the T-REMUS missions were not programed to conduct frequent full plume depth profiles. Specifically, the 0–50 m bin had the highest  $\overline{\varepsilon_o}$  value at  $3\times 10^{-5}~\text{m}^2/\text{s}^3$ , which was within a factor of three compared to the corresponding  $\overline{\varepsilon_m}$  estimate of  $10^{-4}~\text{m}^2/\text{s}^3$ .  $\overline{\varepsilon_o}$  values beyond 100 m from the front mostly ranged between  $10^{-7}~\text{m}^2/\text{s}^3$  and  $10^{-6}~\text{m}^2/\text{s}^3$ , consistent with  $\overline{\varepsilon_m}$  estimates. For estimates in the ambient LIS,  $\overline{\varepsilon_o}$  was almost always far below  $\overline{\varepsilon_m}$ , since overturns form more rarely in this nearly vertically homogeneous layer. The small number of overturns observed in each ensemble in the ambient were also responsible for the very large confidence limits.

The data of Run 1 produced less consistent  $\overline{\varepsilon_{\varrho}}$  estimates, as seen in Fig. 7c, including a poorly resolved TKE dissipation rate peak in the near-frontal region. Even though the ensemble sizes in Run 1 are bigger than in Run 3, the random T-REMUS oscillations about the target depth had a smaller amplitude. Therefore, any existing large overturns in Run 1 that exceeded the vertical oscillation distance of the T-REMUS would not have been included in the  $\overline{\varepsilon_o}$  calculation, because the actual vertical scale of the overturn would not have been resolved. This may have resulted in a significant underestimation of the dissipation rate by the overturn calculations, although the use of a lognormally distributed averaging approach should generally account for the omission of the largest overturns. An alternative interpretation is that larger overturns may be suppressed in the near front region because turbulence is generated by a convective mechanism related to downwelling at the front, rather than the formation of stratified-shear instabilities resulting in initial overturning events on the order of the Ozmidov scale (e.g., MacDonald et al., 2013).

The exponential decay observed by *O'Donnell* et al. [2008] in the Connecticut River and by *Horner-Devine* et al. [2013] in the Merrimack River is plotted as a dashed yellow line in Fig. 7c and d. The decay scale of 15 m is in reasonable agreement with the observed decay of  $\varepsilon_m$  data in the first 100 m behind the front for both Run 1 and Run 3.

The scaling of turbulence using the outer velocity and length scales associated with downwelling at the front is given by  $\varepsilon_1^{'} \sim \frac{w_f^3}{H}$  [e.g., Taylor, 1932; Vassilicos, 2015] where w  $_f$  is the mean downwelling velocity at the front, and H the vertical extent of downwelling which was defined as the deepest extent of the w=-0.1 m/s contour. Scaled  $\varepsilon$  values were averaged among all transects of Run 1 and Run 3 and equaled  $6\times 10^{-4}$  m $^2/s^3$  and  $3\times 10^{-4}$  m $^2/s^3$  respectively, which are very close to the observed TKE dissipation rates in the first 10 m behind the front (Fig. 7c and d). The comparable values between observed and scaled  $\varepsilon$  corroborate that convective instabilities are the dominate

source of turbulence in the frontal head region. Richardson number profiles based on the data shown in Fig. 4 (not shown) are poorly resolved but suggest that conditions are generally unfavorable (i.e., Ri > 10–100) for shear production mechanisms to play an important role in the generation of turbulence within the frontal region. This, in combination with consistency between the convective scaling estimates and observations strongly suggest that downwelling and convective processes are the key drivers of turbulence in this region, with shear production mechanisms playing a more dominant role further from the front.

#### 4.3. Parameterization of frontal turbulence

Previous studies [e.g., O'Donnell et al., 2008; Kilcher and Nash, 2010] have shown that large river systems generate more energetic plumes with more vigorous frontal mixing that result in greater TKE dissipation rates compared to mid-sized or small river systems. To better compare the cross-front distribution of TKE dissipation rates among a wide range of river plumes, we nondimensionalized our dissipation estimates and those from four previous studies using the turbulence scaling of  $\varepsilon_1$ '. This scaling represents the kinetic energy dissipation rate associated with the largest eddies in a turbulent shear flow, analogous to ΔU ^3/L [Vassilicos, 2015; Kundu and Cohen, 2004], where L is the length of the largest eddies and  $\Delta U$  the velocity difference across L, which, for the outer length scales, has the same order of magnitude as the turbulent velocity fluctuations [Kundu and Cohen, 2004]. Thus, when we assign L to the size of the turbulent core of any frontal head and  $\Delta U$  to a representative velocity in that turbulent core, we can scale the TKE dissipation rate to these characteristics.

Data from two studies in the Columbia River plume, *Orton & Jay* [2005] and *Kilcher & Nash* [2010], were incorporated into this study to represent large river systems. To normalize dissipation rates from *Orton & Jay* [2005], we extracted mean  $\epsilon$  values from their Fig. 4, and estimated that H and w were 20 m and 0.25 m/s respectively by interpreting the velocity field vectors and vertical velocity profile of their Fig. 2b. We also extracted TKE dissipation rates from the microstructure profiles of Fig. 4c in *Kilcher & Nash* [2010] and averaged them across the plume thickness. H and w were assumed to be the same as those estimated in *Orton & Jay* [2005].

Data representing mid-sized river systems were incorporated from the studies of O'Donnell et al. [2008] in the Connecticut River plume, and from Luketina and Imberger [1989] in the Leschenault Estuary thermal plume. TKE dissipation estimates of vessel transect Sections 1, 3, and 4 were extracted from Figure 10 in O'Donnell et al. [2008]. H and w were assumed to be comparable to the values calculated during our field program, approximately 3.5 m and 0.12 m/s respectively. To normalize data from Luketina and Imberger [1989], we extracted  $\epsilon$  from their microstructure profiles seen in their Figure 9. Then, values above 2 m depth, the approximate plume thickness, were averaged. Values for H and w, approximately 4.5 m and 0.1 m/s respectively, were estimated using the streamlines plotted in Luketina and Imberger [1987] Figure 13, which displays data that were collected the same day as the microstructure profiles. Representative data from all studies are compiled in Table 2.

In log-log space (Fig. 8) the nondimensionalized TKE dissipation rates from all studies show a uniform decay with distance away from the front. This indicates that, once adjusted for frontal region magnitudes,  $\epsilon$  diminishes at the same rate with increasing normalized distance away from the front  $\left(\frac{x}{H}\right)$ , and therefore, this line represents a more general form of the decay scale  $L_G$ . Data points from the large and smaller river systems approximately collapsed along a line of the form:  $\frac{\epsilon}{\epsilon 1'}=10^{-1.42}*\frac{x}{H}=1.54$  with an  $R^2$  of 0.77 using a Model 2 fit.

 Table 2

 River system parameters used for nondimensionalizing TKE dissipation rates for four previous studies in addition to this one.

Location →		Columbia River	Columbia River	Leschenault Estuary	Connecticut River	Connecticut River This study
Parameter \( \) Symbol/units		Kilcher & Nash [2010]	Orton & Jay [2005]	Luketina and Imberger [1989]	O'Donnell et al., [2008]	
River discharge	$Q_r \left[ \frac{m^3}{s} \right]$	4000	4800	Х	1192	388
tidal amplitude	$A_t[m]$	2.26	2.5	0.4	0.73	0.97
volumetric flux due to tidal prism	$U_t\left[\frac{m}{s}\right]$	1.35	1.43	0.75	0.36	0.56
river mouth width	$W_m[m]$	2000	2000	120	600	600
river mouth depth	$h_m[m]$	15	15	3.5	6	6
vertical extent of frontal downwelling	H[m]	20	20	4.5	3.5	3.5
mean frontal downwelling velocity	$w_f\left[\frac{m}{s}\right]$	0.25	0.25	0.1	0.12	0.12

#### 5. Summary

The T-REMUS was successful in sampling the energetic region of the Connecticut River plume front. It gathered high resolution and synchronous hydrographic, microstructure, and velocity data over multiple cross-front transects, which enabled us to produce a more detailed description of frontal structure and turbulent mixing than previous studies.

These observations corroborate the existing views on river plume fronts and their laboratory equivalents. For example, the frontal region was found to have the internal structure of a classical gravity current as described in *Simpson* [1982] and Britter & Simpson [1978], and the

frontal circulation patterns aligned with those observed in the Leschenault estuary outfall by Luketina and Imberger [1987] and in the Chesapeake Bay plume by Marmorino and Trump, 2000. These circulation patterns consisted of strong downwelling at the front of order 0.1 m/s, a rotating cell within the frontal head that extended to a depth three times greater than the plume depth in the stable plume interior, and a thin buoyant layer at the surface of mostly horizontal flow that accelerated as it neared the front. Our estimates of TKE dissipation and the decay scale  $L_G$  were consistent with those calculated for the Connecticut River plume front by *O'Donnell* et al. [2008], as well as with those calculated for the Merrimack River by *Horner-Devine* et al. [2013].

Our observational program allowed us to sample the front starting at

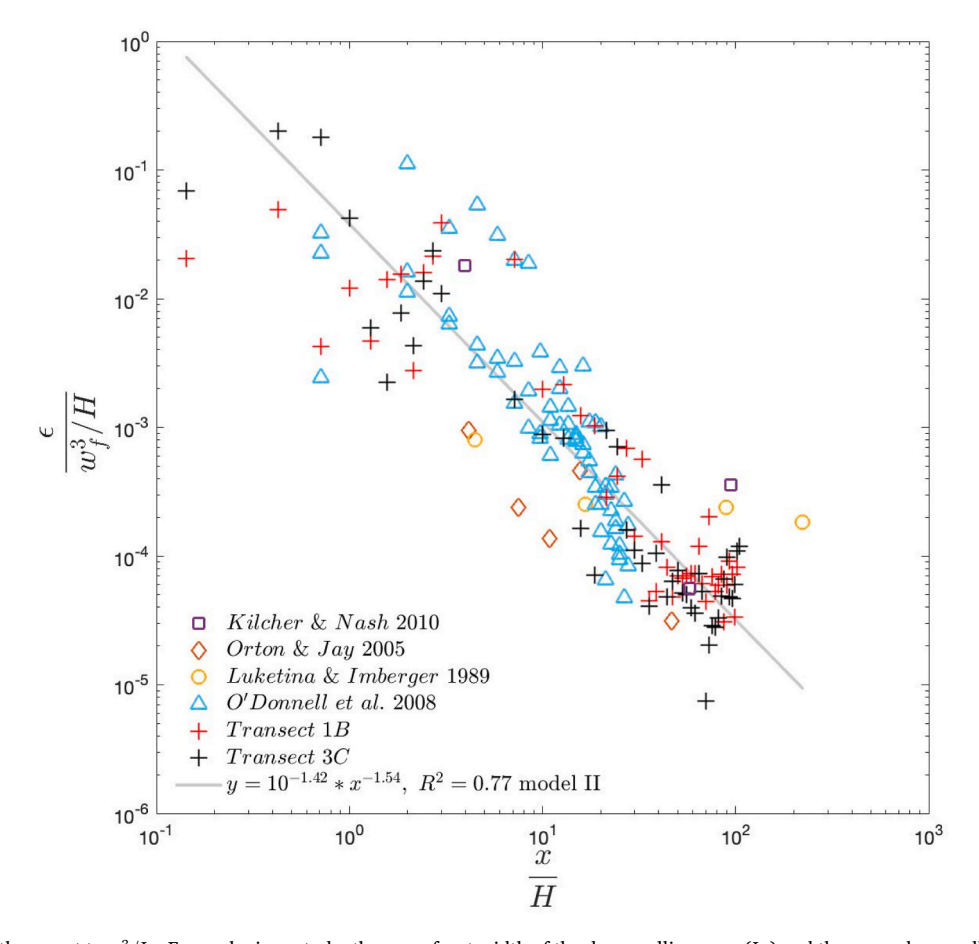


Fig. 8. ε normalized with respect to  $w_f^3/L_h$ . For each given study, the cross-front width of the downwelling zone ( $L_h$ ) and the mean downwelling velocity at the front,  $w_f$  were constant. The linear regression in log-log space was calculated using all available data and is represented by the grey line.

late ebb until mid-flood flow and as it evolved from a lateral front to one that was in the leading edge of the plume. Comparative analysis between these two types of fronts was made possible by numerical models of the Columbia River plume [Akan et al., 2018], but our study is the first to present side by side comparisons using field data.

There was no substantial variation in the magnitude and cross-front distribution of turbulence despite three types of observable change: (1) an overall transformation in the velocity field internal to the plume due to the obliqueness of the front relative to plume propagation direction, (2) an increase in velocity of the underlying ambient LIS due to tidal forcing, and (3) an increased distance of the front away from source waters (5 km). This lack of substantial variation was observed in the near-frontal region, which was consistently comprised of a strongly convective downwelling zone O (10 m), followed by an adjustment region we have termed the trailing frontal zone O (100 m). Beyond the trailing frontal zone is the broad stable interior region of the plume that develops seaward of the lift-off region [MacDonald et al., 2007].

Expecting to see weakening of frontal energetics with distance away from the mouth, as reported by *O'Donnell* et al. [2008], it was surprising to find that the volume occupied by the turbulent core and elevated TKE dissipation rates was largely unchanged. Compared to other river plume systems, the Connecticut plume front is highly influenced by ambient tidal currents, and thus undergoes much more rapid stretching in the alongshore direction than its expansion in the offshore direction due to density current propagation. Ultimately, this gives the plume the appearance of an advancing bore. These characteristics of the plume likely contribute to the maintenance of frontal structure and energetics as the plume advances.

The rate at which TKE dissipation decayed with distance from the front also did not vary substantially during the 3.5-h sampling period. Turbulence was found to be strong and fully isotropic only in the first 5–10 m behind the front which corresponds to the cross-front width of the turbulent core and downwelling zone. Good agreement between scaled and observed  $\varepsilon$  values in the 0–5 m range, suggests that convective instabilities were the generating mechanism of turbulence in the frontal head while advection of turbulence away from the front was not substantial.

A broader non-dimensional comparison with plume data from a variety of other systems suggests that scaling TKE dissipation rates with near-front parameters yields results that are described well by a power law and illustrates that characteristics of frontal structure, such as frontal zone width and downwelling velocity, correlate well with turbulence in both the downwelling and trailing frontal zones.

#### CRediT authorship contribution statement

Nikiforos Delatolas: Writing – review & editing, Writing – original draft, Visualization, Validation, Methodology, Investigation, Formal analysis, Data curation. Daniel G. MacDonald: Writing – review & editing, Supervision, Resources, Project administration, Methodology, Investigation, Funding acquisition, Conceptualization. Louis Goodman: Supervision, Methodology. Michael Whitney: Writing – review & editing, Resources, Investigation, Funding acquisition, Conceptualization. Kimberly Huguenard: Writing – review & editing, Investigation, Funding acquisition, Conceptualization. Kelly Cole: Funding acquisition, Conceptualization, Conceptualization.

# **Declaration of competing interest**

The authors declare the following financial interests/personal relationships which may be considered as potential competing interests:

Daniel MacDonald reports financial support was provided by National Science Foundation. Michael Whitney reports financial support was provided by National Science Foundation. Kelly Cole reports financial support was provided by National Science Foundation.

#### Data availability

Data will be made available on request.

#### Acknowledgements

This project was funded by National Science Foundation Awards OCE-1756599, OCE-1756578, and OCE-1756690.

#### References

- Akan, Ç., McWilliams, J.C., Moghimi, S., Özkan-Haller, H.T., 2018. Frontal dynamics at the edge of the Columbia River plume. Ocean Model. 122, 1–12.
- Britter, R.E., Simpson, J.E., 1978. Experiments on the dynamics of a gravity current head. J. Fluid Mech. 88 (2), 223–240.
- Cole, K.L., MacDonald, D.G., Kakoulaki, G., Hetland, R.D., 2020. River plume sourcefront connectivity. Ocean Model. 150, 101571.
- Ellison, T.H., 1957. Turbulent transport of heat and momentum from an infinite rough plane. J. Fluid Mech. 2 (5), 456–466.
- Ellison, T.H., Turner, J.S., 1959. Turbulent entrainment in stratified flows. J. Fluid Mech. 6 (3), 423–448.
- Ferron, B., Mercier, H., Speer, K., Gargett, A., Polzin, K., 1998. Mixing in the Romanche fracture zone, J. Phys. Oceanogr. 28 (10), 1929–1945.
- Garvine, R.W., 1974. Dynamics of small-scale oceanic fronts. J. Phys. Oceanogr. 4 (4), 557–569.
- Garvine, R.W., Monk, J.D., 1974. Frontal structure of a river plume. J. Geophys. Res. 79 (15), 2251–2259.
- Goodman, L., Levine, E.R., Lueck, R.G., 2006. On measuring the terms of the turbulent kinetic energy budget from an AUV. J. Atmos. Ocean. Technol. 23 (7), 977–990.
- Horner-Devine, A.R., Chickadel, C.C., MacDonald, D.G., 2013. Coherent structures and mixing at a river plume front. Coherent Flow Structures at Earth's Surface 359–369.
- Horner-Devine, A.R., Hetland, R.D., MacDonald, D.G., 2015. Mixing and transport in coastal river plumes. Annu. Rev. Fluid Mech. 47, 569–594.
- Imberger, J., 1983. Tidal jet frontogenesis. Trans. Inst. Eng. Aust. Mech. Eng. 8 (4), 171–180.
- Imberger, J., & Luketina, D. (1988). Turbulent motions in a surface buoyant jet. In Stratified Flows (pp. 755-771). ASCE.
- Itsweire, E.C., Helland, K.N., Van Atta, C.W., 1986. The evolution of grid-generated turbulence in a stably stratified fluid. J. Fluid Mech. 162, 299–338.
- Itsweire, E.C., Koseff, J.R., Briggs, D.A., Ferziger, J.H., 1993. Turbulence in stratified shear flows: implications for interpreting shear-induced mixing in the ocean. J. Phys. Oceanogr. 23 (7), 1508–1522.
- Jirka, G.H., Arita, M., 1987. Density currents or density wedges: boundary-layer influence and control methods. J. Fluid Mech. 177, 187–206.
- Kilcher, L.F., Nash, J.D., 2010. Structure and dynamics of the Columbia River tidal plume front. J. Geophys. Res.: Oceans 115 (C5).
- Kolmogorov, A.N., 1941. The local structure of turbulence in incompressible viscous fluid for very large Reynolds numbers. Proceedings of the USSR Academy of Science 30, 301–305.
- Kundu, P.K., Cohen, I.M., 2004. Fluid Mechanics, third ed. Elsevier Academic Press, Boston, MA.
- Large, W.G., Pond, S., 1981. Open ocean momentum flux measurements in moderate to strong winds. J. Phys. Oceanogr. 11 (3), 324–336.
- Levine, E.R., Goodman, L., O'Donnell, J., 2009. Turbulence in coastal fronts near the mouths of block Island and long Island sounds. J. Mar. Syst. 78 (3), 476–488.
- Lueck, R.G., 2016. Calculating the rate of dissipation of turbulent kinetic energy. Rockland Scientific International Technology 18. *Note TN-028*.
- Luketina, D.A., Imberger, J., 1987. Characteristics of a surface buoyant jet. J. Geophys. Res.: Oceans 92 (C5), 5435–5447.
- Luketina, D.A., Imberger, J., 1989. Turbulence and entrainment in a buoyant surface plume. J. Geophys. Res.: Oceans 94 (C9), 12619–12636.
- MacDonald, D.G., Carlson, J., Goodman, L., 2013. On the heterogeneity of stratified-shear turbulence: observations from a near-field river plume. J. Geophys. Res.: Oceans 118 (11), 6223–6237.
- MacDonald, D.G., Goodman, L., Hetland, R.D., 2007. Turbulent dissipation in a near-field river plume: a comparison of control volume and microstructure observations with a numerical model. J. Geophys. Res.: Oceans 112 (C7).
- Marmorino, G.O., Trump, C.L., 2000. Gravity current structure of the Chesapeake Bay outflow plume. J. Geophys. Res.: Oceans 105 (C12), 28847–28861.
- Miles, J.W., 1961. On the stability of heterogeneous shear flows. J. Fluid Mech. 10 (4), 496–508
- O'Donnell, J. (1997). Observations of near-surface currents and hydrography in the Connecticut River plume with the surface current and density array. J. Geophys. Res.: Oceans, 102(C11), 25021-25033.
- O'Donnell, J., Ackleson, S.G., Levine, E.R., 2008. On the spatial scales of a river plume. J. Geophys. Res.: Oceans 113 (C4).
- Orton, P.M., Jay, D.A., 2005. Observations at the tidal plume front of a high-volume river outflow. Geophys. Res. Lett. 32 (11).
- RGL Consulting Ltd., 2003. REMUS Microstructure Measurement System. RGL CONSULTING LTD (Technical manual.
- Simpson, J.E., 1982. Gravity currents in the laboratory, atmosphere, and ocean. Annu. Rev. Fluid Mech. 14 (1), 213–234.

- Simpson, J.E., Britter, R.E., 1979. The dynamics of the head of a gravity current advancing over a horizontal surface. J. Fluid Mech. 94 (3), 477–495.
- Spicer, P., Cole, K.L., Huguenard, K., MacDonald, D.G., Whitney, M.M., 2021. The effect of bottom-generated tidal mixing on tidally pulsed river plumes. J. Phys. Oceanogr. https://doi.org/10.1175/JPO-D-20-0228.1.
- Taylor, G.I., 1932. The transport of vorticity and heat through fluids in turbulent motion. Proc. R. Soc. Lond. - Ser. A Contain. Pap. a Math. Phys. Character 135 (828), 685–702.
- Thorpe, S.A., 1977. Turbulence and mixing in a Scottish loch. Phil. Trans. Roy. Soc. Lond. Math. Phys. Sci. 286 (1334), 125–181.
- Vassilicos, J.C., 2015. Dissipation in turbulent flows. Annu. Rev. Fluid Mech. 47, 95–114.
   Whitney, M.M., Jia, Y., Cole, K.L., MacDonald, D.G., Huguenard, K.D., 2021. Freshwater composition and connectivity of the Connecticut River Plume during ambient flood tides. Front. Mar. Sci. 8, 747191 https://doi.org/10.3389/fmars.2021.747191.